
MQuant: Unleashing the Inference Potential of Multimodal Large Language Models via Full Static Quantization

JiangYong Yu^{1*} Sifan Zhou^{1,2,*†} Dawei Yang^{1◇} Shuo Wang¹ Shuoyu Li^{1,3†}
 Xing Hu¹ Chen Xu¹ Zukang Xu¹ Changyong Shu¹ Zhihang Yuan¹

Abstract

Multimodal large language models (MLLMs) have garnered widespread attention due to their ability to understand multimodal input. However, their large parameter sizes and substantial computational demands severely hinder their practical deployment and application. While quantization is an effective way to reduce model size and inference latency, its application to MLLMs remains underexplored. In this paper, we propose MQuant, a post-training quantization (PTQ) framework designed to tackle the unique challenges of multimodal large language models (MLLMs). Conventional quantization often struggles with MLLMs because of (a) high inference latency from large visual token counts, (b) distributional disparities between visual and textual tokens, and (c) extreme outliers introduced by Hadamard-based transformations. To address these issues, MQuant introduces: • Modality-Specific Static Quantization (MSQ), assigning distinct static scales for visual vs. textual tokens; • Attention-Invariant Flexible Switching (AIFS), reordering tokens to preserve casual attention while eliminating expensive token-wise scale computations; • Rotation Magnitude Suppression (RMS), mitigating weight outliers arising from online Hadamard rotations. On five mainstream MLLMs (including Qwen-VL, MiniCPM-V, CogVLM2), MQuant under W4A8 achieves near-floating-point accuracy (<1% degradation) while reducing inference latency by up to 30%, significantly outperforming existing PTQ baselines. Our MQuant effectively bridges the gap for efficient and accurate MLLMs inference in resource-constrained devices. [code](#) will be released.

◇Corresponding author, *Equal contribution, †This work was conducted during his internship at Houmo. ¹Houmo AI ²Southeast University ³Xi'an Jiaotong University. Correspondence to: Dawei Yang <>.

1. Introduction

Recent advances in large language models (LLMs) (Brown et al., 2020; Touvron et al., 2023a;b; Dubey et al., 2024) have led to remarkable performance on a wide range of natural language processing tasks. However, these models often struggle when dealing with non-textual data such as images or videos. Multimodal large language models (MLLMs) (Reid et al., 2024; Achiam et al., 2023b; Wang et al., 2023) address this limitation by integrating visual and textual modalities, thereby enabling more comprehensive understanding and reasoning. Despite these benefits, their large parameter sizes, coupled with substantial computational demands, poses a major challenge for real-world deployment, particularly in resource-constrained or privacy-sensitive environments.

Challenges in MLLM Quantization. Quantization has proven an effective strategy for reducing memory usage and inference costs in LLMs (Yuan et al., 2023a; Shao et al., 2023), by converting high-precision parameters (e.g., FP32) into lower-bit representations (e.g., INT8). Yet, the transition from LLMs to MLLMs brings three unique difficulties:

1. **Time-to-First-Token (TTFT) Explosion.** MLLMs often generate large numbers of visual tokens (e.g., patch embeddings or region proposals) with the resolution and aspect ratio of input images or videos. As shown in Fig 1(a), in models such as Qwen2-VL (Wang et al., 2024), the number of prefill visual tokens grows as image resolution increases (detailed figure in Fig. 7). As image or video resolution increases, the prefill visual tokens can escalate dramatically—leading to high TTFT and negatively impacting latency-sensitive tasks. Moreover, in higher-demand scenarios such as video-based tasks and multi-image dialogues, the accumulation of visual tokens becomes even more pronounced, further exacerbating the increase in TTFT. Per-token dynamic quantization, though flexible, exacerbates this overhead by computing scale factors token-by-token.
2. **Disparate Modality Distributions.** As shown in Fig 1 (b), the activation distributions between visual and textual tokens reveal substantial numerical discrepancies, where visual token activations can span a significantly

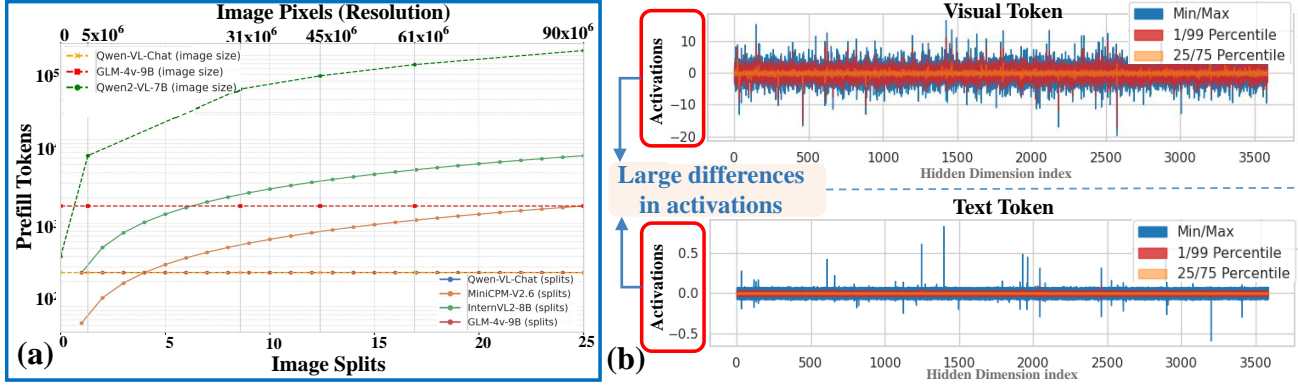


Figure 1: (a) The number of prefill visual tokens across different MLLMs as the image splits or resolution increases. (b) The activation values of visual tokens range from -20 to 10 , whereas textual tokens are centered around 0 , with only a few having absolute magnitudes exceeding 0.5 .

broader range (e.g., -20 to 10) than textual tokens, which typically center near 0 . A single global scale factor for both visual and textual tokens leads to either aggressive clipping of visual outliers or increased quantization granularity for text, harming overall accuracy.

- Visual Outliers.** High-magnitude outliers in visual tokens, often reflecting salient image regions, make traditional clipping-based methods unsuitable. Naively clipping these outliers can cause severe accuracy drops, illustrated in Table 1.

Table 1: Ablations on the clip range for different tokens.

Clip Range	Bits (W/A)	Visual Tokens	Textual Tokens
-	BF16 / BF16	61.40	
(0-1.0)	BF16 / INT16	61.20 ($\downarrow 0.20$)	61.25 ($\downarrow 0.15$)
(0-0.99999)	BF16 / INT16	18.92 ($\downarrow 42.48$)	60.09 ($\downarrow 1.31$)

Our Approach. To tackle these challenges, we propose *MQuant*, an accurate and efficient *post-training quantization* (PTQ) framework *specifically tailored to MLLMs*. Our contributions center around:

- Modality-Specific Static Quantization (MSQ)** and **Attention-Invariant Flexible Switching (AIFS)**, which apply distinct per-tensor scales for visual vs. textual tokens and reorder multimodal inputs to avoid repeated, token-wise scale computation. By doing so, *MQuant* slashes TTFT and preserves accuracy.
- Rotation Magnitude Suppression (RMS)** for mitigating fresh outliers introduced by online Hadamard rotations. Our theoretical analysis reveals the emergence of large-mean channels in MLLM weights, and RMS effectively reduces these outliers with minimal overhead.

Experimental Results and Impact. We evaluate *MQuant* on five mainstream MLLMs—InternVL (Chen et al., 2024a), Qwen-VL (Bai et al., 2023b), MiniCPM-V (Yao

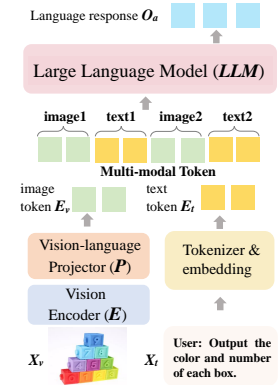
et al., 2024), CogVLM2 (Hong et al., 2024), and Qwen2-VL (Wang et al., 2024)—over multiple vision-language benchmarks. Under a W4A8 setting, *MQuant* routinely maintains $> 98\%$ of the floating-point accuracy, significantly outperforming baseline quantization methods. In addition, our modality-specific approach and token reordering reduce inference latency by effectively handling thousands of visual tokens at scale. We will release `code` to facilitate further development and encourage real-world adoption in resource-limited scenarios.

In summary, *MQuant* is, to our knowledge, the first PTQ framework *explicitly* designed for MLLMs, demonstrating both near-lossless performance and reduced computational demands at lower bit-widths. We hope our method paves the way for broader, faster, and more efficient multimodal LLM deployments.

2. Preliminaries

2.1. MLLMs Architecture and Models

As shown in the Figure, the existing MLLMs framework (Bai et al., 2023b; Chen et al., 2024b) mainly consists of three modules: a vision encoder E for processing visual inputs, a visual-language projector P that serves as a bridge to align the two modalities and a large language model (*LLM*) that handles the multi-modal tokens and performs reasoning.



Vision Encoder. Taking the input image or video X_v as input and compressing the original vision information into more compact patch features F_v . This process typically utilizes a Vision Transformer (ViT) (Dosovitskiy, 2021), such as CLIP (Radford et al., 2021) and OpenCLIP (Ilharco

et al., 2021). It can be formulated as: $F_v = E(\mathbf{X}_v)$.

Vision-Language Projector. The task of the vision-language projector P is to map the visual patch features F_v into the textual feature space: $E_v = P(F_v)$.

Large Language Model. The pre-trained large language model is the core component of MLLMs, endowing the framework with exceptional capabilities, such as zero-shot generalization, instruction following, and in-context learning. Typically, a text tokenizer is integrated with the LLM, mapping text prompts \mathbf{X}_t to the text tokens \mathbf{E}_t . The text tokens \mathbf{E}_t and the visual tokens \mathbf{E}_v are then concatenated to form the input for MLLMs, which outputs the final response sequence \mathbf{O}_a in an autoregressive manner:

$$LLM(\mathbf{O}_a | \mathbf{E}_v, \mathbf{E}_t) = \prod_{i=1}^l LLM(y_i | \mathbf{E}_v, \mathbf{E}_t, y_{<i}) \quad (1)$$

where l denotes the length of \mathbf{O}_a . The parameter sizes of large language models (LLMs) range from 3 billion to tens of billions. Commonly used open-source LLMs include the Llama series (Touvron et al., 2023a;b), Qwen (Bai et al., 2023a), InternLM (Cai et al., 2024), MiniCPM (Hu et al., 2024a), ChatGLM (GLM et al., 2024).

These foundational elements of MLLMs have benefited significantly from the rapid advancements in LLM technology. Flamingo (Alayrac et al., 2022) pioneered connecting pre-trained visual encoders to LLMs, demonstrating strong generalization across visual-language tasks. Following the emergence of ChatGPT (Achiam et al., 2023a), numerous open-source models based on pre-trained LLMs like LLaMA (Touvron et al., 2023a) and its variants (Touvron et al., 2023b; Zheng et al., 2024) have been proposed (Li et al., 2023; Huang et al., 2024; Zhu et al., 2023; Liu et al., 2024). Subsequent efforts like Qwen-VL (Bai et al., 2023b), InternVL (Chen et al., 2024b), and CogVLMV2 (Hong et al., 2024) enhanced MLLMs from perspectives such as high-resolution input and larger-scale training data. However, the substantial parameters of MLLMs lead to high computational costs, limiting broader application. Recently, smaller MLLMs like Mini-Gemini (Li et al., 2024), MobileVLM (Chu et al., 2024), and MiniCPM-V (Yao et al., 2024) have emerged. Despite these developments, dedicated quantization methods for MLLMs to further reduce memory usage and accelerate inference remain under-explored.

2.2. Post Training Quantization (PTQ)

PTQ serves as a potent strategy for model compression. By converting the high-precision variables of pre-trained models into low-bit integers, it achieves a reduction in memory usage and an acceleration of inference speed. For uniform quantization, given a floating-point (FP) tensor x (weights or activations), it can be uniformly quantized to b -bits in signed quantization as follows:

$$\hat{\mathbf{x}} = \mathbf{Q}_U(\mathbf{x}, b) = (\text{clamp}(\lfloor \frac{\mathbf{x}}{s} \rfloor + z, q_{min}, q_{max}) - z) \cdot s \quad (2)$$

where $s = \frac{\max(|\mathbf{x}|)}{2^{b-1}-1}$ is the scale factor, $\lfloor \cdot \rfloor$ is the rounding-to-nearest operator, and the function $\text{clamp}(\cdot)$ clips values outside the integer range $[q_{min}, q_{max}]$. z is zero-point. s denotes the quantization scale factor, which reflects the proportional relationship between FP values and integers. $[q_{min}, q_{max}]$ is the quantization range determined by the bit-width b . Generally, when we quantize the network’s weight with 4-bit and activations with 8-bit, called it as W4A8. We can calculate s offline using the activations from calibration samples, known as **static quantization**. We can also use the runtime statistics of activations to get s , referred to as **dynamic quantization**. More details are in Appendix A.12.

Existing post-training quantization (PTQ) methods for LLMs are categorized into weight-only and weight-activation quantization (Zhao et al., 2023; Yuan et al., 2024; Shang et al., 2023; Yue et al., 2024; Hu et al., 2024b; 2025). Weight-only methods like GPTQ (Frantar et al., 2022), QuIP (Chee et al., 2024), and AWQ (Lin et al., 2023) achieve high compression rates but offer limited inference acceleration. In contrast, weight-activation quantization methods (Xiao et al., 2022; Wei et al., 2022; Yuan et al., 2023b; Zhang et al., 2024) quantize both weights and activations, improving memory usage and latency. The main challenge is activation outliers causing quantization errors. Techniques like SmoothQuant (Xiao et al., 2022) shift quantization difficulty from activations to weights, while OmniQuant (Shao et al., 2023) optimizes performance by training quantization parameters. SliceGPT (Ashkboos et al., 2024a) reduces memory demands by designing a Pre-LN + Rotate Scheme for LLMs sparsification based on computational invariance. They achieve this by adding a linear layer in the residual connection (see Appendix A.14). Unlike SliceGPT, we further develop a Post-LN + Rotate scheme to accommodate more vision encoder and extends its applicability to various MLLMs. This enhancement broadens the the LayerNorm + Rotate approach, making it suitable for both Pre-LN and Post-LN configurations across various MLLMs. Recently, Quarot (Ashkboos et al., 2024b) introduces rotations to eliminate outliers; however, this solution is not applicable to MLLMs due to inherent modality differences.

3. Method

In this section, we present *MQuant*, a post-training quantization solution specifically designed for MLLMs. In Sec. 3.1, we describe modality-specific static quantization (MSQ) and attention-invariant flexible switching (AIFS). In Sec. 3.2, we identify the weight outliers caused by the online Hadamard rotations and state Rotation Magnitude Suppression (RMS). We provide the detailed MQuant algorithm for FP MLLMs in Appendix A.1 Algorithm 1.

3.1. Modality-Specific Static Quantization and Attention-Invariant Flexible Switching

Motivation and Overview. Multi-modal Large Language Models (MLLMs) often generate a large number of visual tokens. As discussed in Section 1, the number of these tokens increases rapidly with higher image or video resolution (see Fig. 1(a)). This growth causes high inference latency when using per-token dynamic quantization, due to expensive token-wise scale computations. Such computations are not ideal for mobile or embedded devices. In contrast, static per-tensor quantization bypasses the need for repeated scale updates and offers much lower overhead. However, naïvely applying per-tensor quantization to both text and visual tokens can degrade accuracy, because their activation distributions differ significantly (Fig. 1(b)).

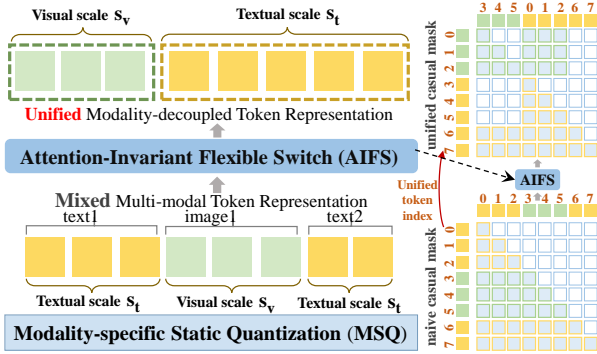


Figure 2: Overview of Modality-Specific Static Quantization (MSQ) and Attention-Invariant Flexible Switching (AIFS). AIFS reorders tokens so that all visual tokens appear first, then the textual tokens, while adjusting the causal mask to preserve the original model logic.

We address this issue with a two-part method: (1) *Modality-Specific Static Quantization (MSQ)* and (2) *Attention-Invariant Flexible Switching (AIFS)*. MSQ applies different static scaling factors for visual and textual tokens, while AIFS reorders their positions to avoid irregular data slicing. Our method retains accuracy while benefiting from the efficiency of per-tensor quantization, especially for high-resolution inputs.

Modality-Specific Static Quantization (MSQ). Let E be an input sequence of length L that intermixes textual and visual tokens. Denote $E = \{e_1^t, \dots, e_{m-1}^t, e_m^v, \dots, e_n^v, e_{n+1}^t, \dots, e_L^t\}$, where m, n specify the visual token segment. We observe that visual tokens often have larger activation magnitudes, which can overshadow textual features. To handle these differences, we apply two distinct sets of *static per-tensor* quantization

parameters:

$$E = \underbrace{(e_1^t, \dots, e_{m-1}^t)}_{\text{text scale } s_t} \underbrace{(e_m^v, \dots, e_n^v)}_{\text{visual scale } s_v} \underbrace{(e_{n+1}^t, \dots, e_L^t)}_{\text{text scale } s_t}. \quad (3)$$

Here, s_v denotes the scale factor for visual tokens, while s_t is for textual tokens. By calibrating s_v and s_t *once* before inference, we avoid the overhead of per-token scale estimation. This design aligns well with hardware that favors simple per-tensor quantization. It also prevents large visual values from saturating the narrower distribution of textual tokens.

Attention-Invariant Flexible Switching (AIFS). Despite the benefits of MSQ, it complicates data handling if textual and visual tokens remain interleaved in E . Naïve slicing and concatenating at runtime can increase memory traffic and reduce efficiency for GEMM-based layers like QK and FC. To overcome this, we propose *Attention-Invariant Flexible Switching (AIFS)*. Figure 2 illustrates the idea: we *reorder* the sequence so that all visual tokens appear first, followed by textual tokens. We then alter the causal mask to preserve the original auto-regressive relationships.

Causal attention (Vaswani et al., 2017) ensures each token can only attend to earlier tokens. Formally, for a naive sequence E , the attention matrix is

$$\mathbf{A} = \text{Softmax}\left(\frac{\mathbf{Q}\mathbf{K}^\top}{\sqrt{D}} + M_{i,j}\right), \quad M_{i,j} = \begin{cases} 0, & \text{if } j \leq i, \\ -\infty, & \text{otherwise.} \end{cases} \quad (4)$$

With AIFS, we reorder E into $E^u = \{e_m^v, \dots, e_n^v, e_1^t, \dots, e_{m-1}^t, \dots, e_{n+1}^t, \dots, e_L^t\}$ and obtain a *unified causal mask* $M_{i,j}^u$:

$$M_{i,j}^u = \begin{cases} 0 & \text{if one of the following conditions is met:} \\ & (i \leq (n-m), j \leq i \text{ or } (n-m) < j \leq n) \\ & \text{or } ((n-m) < i \leq n, (n-m) < j \leq i) \\ & \text{or } (i > n, j \leq i) \\ -\infty & \text{otherwise} \end{cases} \quad (5)$$

The position embeddings are also shifted consistently. More details can be found in the Appendix A.2. This guarantees that *attention scores remain numerically equivalent* to the original sequence. Thus, token reordering does not change the auto-regressive logic, but it *does* simplify memory operations so that we can feed all visual tokens through a single static-scale multiplication and do the same for textual tokens.

Efficiency and Practical Benefits. Our experiments in Section 4 show that MSQ plus AIFS delivers three main advantages:

- *High Compatibility and Strong Theoretical Equivalence:* The causal-mask transformation ensures that the model’s output is numerically the same as if tokens were not reordered. This reordering can be integrated into existing MLLM implementations without major code changes.
- *Reduced Inference Latency:* We replace per-token dynamic quantization with a static per-modality approach. This removes the need to recalculate scales per token, cutting runtime overhead and boosting throughput.
- *Enhanced Memory Efficiency:* Placing all visual tokens first avoids repeated slicing or padding of interleaved tokens. We can handle them with a single global scale factor (s_v), then switch to s_t for textual tokens. This reduces memory usage. We observe up to 24.7% speedups and 152.9% memory gains (see Table 11).

In summary, *MSQ + AIFS* offers a straightforward and effective way to handle the unique challenges of multi-modal token distributions. It is especially valuable on edge devices or other constrained platforms where dynamic quantization is hard to implement at scale, yet per-tensor static quantization is hardware-friendly and fast.

3.2. FHT-Based Weight Outlier Mitigation: Rotation Magnitude Suppression

Background and Motivation. Chee *et al.* (Chee *et al.*, 2024) and Tseng *et al.* (Tseng *et al.*, 2024) introduced *incoherence* to measure the difficulty of quantization. A lower incoherence indicates a simpler quantization scenario. Concretely, let $W \in \mathbb{R}^{m \times n}$ be a weight matrix with singular vectors e_i and e_j . They define

$$|W_{ij}| = |e_i^\top W e_j| \leq \mu \frac{\|W\|_F}{\sqrt{mn}}, \quad (6)$$

where μ is the *incoherence coefficient*. The smaller μ is, the easier it is to quantize W . They also showed that applying a Hadamard transform to both weights and activations can effectively reduce μ . Quarot (Ashkboos *et al.*, 2024b) further applies *offline* Hadamard transforms and a *partially online* Hadamard transform, as shown in Figure 3(a), to achieve state-of-the-art quantization on LLMs.

However, Multi-modal LLMs (MLLMs) combine an LLM component with a *visual encoder*, which often relies on LayerNorm. Quarot’s partial online transform cannot be applied directly to all such norms. Inspired by SliceGPT (Ashkboos *et al.*, 2024a), we convert visual encoders’ LayerNorms into RMSNorms. More details can be found in the Appendix A.14. This change makes Quarot-like Hadamard transforms applicable to MLLMs. Yet, as Table 2 demonstrates, Quarot still underperforms on many MLLM tasks. Tseng *et al.* (Tseng *et al.*, 2024) also proved that *random*

Hadamard transforms (RHT) can reduce incoherence for Hessians and weights, but they did not analyze *online* (fast) Hadamard transforms (FHT). In Quarot, FHT is crucial for low-bit quantization (e.g., 4-bit) as shown in Table 12. We investigate why FHT can yield fresh outliers in MLLMs and propose a method to suppress them.

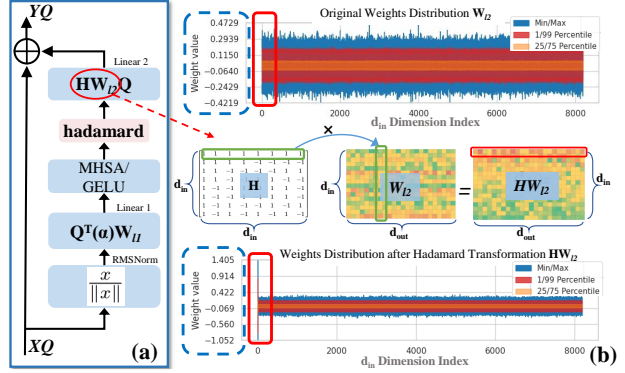


Figure 3: (a) The pipeline of Quarot, showing offline and partially online Hadamard transforms. (b) An MLLM weight matrix where applying an online FHT produces outliers in the first row.

Channel-Mean Outliers in Online FHT. Following (Eq. 6), let $W_{\ell_2} \in \mathbb{R}^{n \times m}$ be a weight matrix. We denote $\|W_{\ell_2}\|_F$ as the Frobenius norm. A Hadamard matrix $H \in \{-1, 1\}^{n \times n}$ with orthonormal rows preserves this norm, i.e., $\|H W_{\ell_2}\|_F = \|W_{\ell_2}\|_F$. Suppose μ_{ℓ_2} is the incoherence coefficient for W_{ℓ_2} , satisfying $\max(|W_{\ell_2}|) = \mu_{\ell_2} \frac{\|W_{\ell_2}\|_F}{\sqrt{mn}}$. Let HW_{ℓ_2} be the transformed weight, and let its incoherence coefficient be $\mu_{H\ell_2}$. Then

$$\frac{\mu_{H\ell_2}}{\mu_{\ell_2}} = \frac{\max |H W_{\ell_2}|}{\max |W_{\ell_2}|}. \quad (7)$$

For many Hadamard transforms, the first row (and first column) contain identical $\frac{1}{\sqrt{n}}$ entries, while other rows sum to zero. Hence, the first channel after transformation is

$$(HW_{\ell_2})_{0j} = \sqrt{n} \text{mean}(w_{:,j}).$$

If the mean is large, the first element in that row can exceed the original maximum and thus raise $\mu_{H\ell_2}$. Concretely, when

$$\sqrt{n} \text{mean}(w_{:,j}) > \max_i (w_{ij}), \quad (8)$$

a new *channel-mean outlier* appears in the first row. Figure 3(b) shows such an occurrence in an MLLM. This issue arises especially in Quarot’s *online* (partial) FHT step, which applies Hadamard rotations per forward pass rather than strictly offline.

Our Approach: Rotation Magnitude Suppression (RMS).

We propose *Rotation Magnitude Suppression (RMS)* to handle these new outliers with minimal overhead. We first identify whether a channel meets (Eq. 8). If it does, we:

1. *Split* the problematic channel from the main GEMM kernel and process it using a separate GEMV.
2. *Zero out* that row in HW_{ℓ_2} so that the main kernel does not double-count it.
3. *Add* the partial output (from the split GEMV) back to the main path before the activation.

Figure 4 shows the workflow. This targeted split ensures large-mean channels do not trigger extreme first-row values during the per-forward-pass FHT. The added cost is small, since only channels meeting Eq. 8 require this procedure.

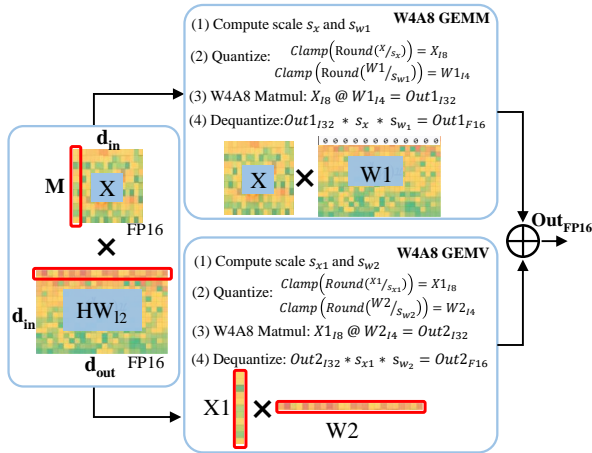


Figure 4: An overview of our **RMS**. We separate outlier-prone channels into a dedicated GEMV path, zero their row in the main kernel, and then merge the results.

Why Not Subtract Channel Means Directly? A straightforward idea is to separate out each channel’s mean before applying H and then re-inject it afterward. However, this leads to two major issues: 1. The separated means are still subject to Hadamard rotation, creating a new linear transformation where the first channel again becomes large. 2. Splitting and then re-injecting the means effectively doubles the linear operations, significantly increasing the computational cost. In contrast, our RMS approach modifies only the row triggering the outlier condition and does not require additional linear layers, thereby offering a more efficient and effective resolution.

Summary. Algorithm 2 outlines how RMS integrates with Quarot’s FHT or other partially online Hadamard transforms. In Table 12, we show that RMS substantially curbs weight outliers in MLLMs under W4A8 quantization, raising accuracy with minimal overhead. Hence, RMS addresses a key

Table 2: Comprehensive quantization results of different MLLMs across various evaluation datasets.

MLLMs	Method	Bits Setting		T.VQA↑	D.VQA↑	OCRb.↑	MME↑
		Visual	LLM				
InternVL2-8B	-	BF16	BF16	77.65	90.97	794	2209
	RTN			52.02	59.04	542	1528
	SQ			59.88	59.75	544	1540
	Quarot	W8A8	W4A8	73.34	84.07	715	2067
	MQuant			77.49	90.27	785	2156
	RTN			40.06	31.58	302	1482
	SQ			46.48	31.21	310	1540
	Quarot	W4A8	W4A8	49.10	33.62	361	1941
MQuant			76.62	88.42	725	2155	
Qwen-VL-Chat-9.6B	-	BF16	BF16	61.40	60.36	493	1834
	RTN			0.45	0.03	189	625
	SQ			7.45	7.70	160	797
	Quarot	W8A8	W4A8	45.32	42.44	286	940
	MQuant			61.16	59.31	483	1691
	RTN			1.02	0.02	193	585
	SQ			8.59	4.28	188	921
	Quarot	W4A8	W4A8	46.77	37.35	289	1091
MQuant			60.50	58.72	473	1713	
MiniCPM-V 2.6-8B	-	BF16	BF16	79.10	89.18	847	2248
	RTN			61.00	65.16	332	1300
	SQ			62.40	65.76	424	1510
	Quarot	W8A8	W4A8	73.71	80.04	736	1850
	MQuant			80.41	89.15	844	2244
	RTN			60.70	62.23	351	1404
	SQ			65.67	60.02	455	1491
	Quarot	W4A8	W4A8	68.96	79.63	685	1734
MQuant			81.14	89.75	839	2189	
Qwen2-VL-7B	-	BF16	BF16	84.43	93.87	842	2319
	RTN			33.92	52.61	442	1298
	SQ			49.11	53.97	444	1500
	Quarot	W8A8	W4A8	79.36	89.57	754	2045
	MQuant			84.43	93.61	830	2269
	RTN			40.20	38.82	422	1082
	SQ			46.25	52.36	411	1535
	Quarot	W4A8	W4A8	71.44	83.96	670	1911
MQuant			84.32	93.58	824	2255	
GLM-4V-9B	-	BF16	BF16	82.82	81.16	782	2153
	RTN			7.05	3.70	0.00	140
	SQ			9.05	4.10	0.00	148
	Quarot	W8A8	W4A8	82.00	80.17	782	2115
	MQuant			82.06	80.53	782	2164
	RTN			7.61	3.60	0.00	163
	SQ			9.85	4.40	0.00	188
	Quarot	W4A8	W4A8	64.16	45.52	516	2048
MQuant			81.58	79.67	754	2120	

shortcoming of online Hadamard transforms by suppressing large-mean channels.

4. Experiments

Models and Datasets. We evaluate our *MQuant* on five MLLMs: InternVL2-8B (Chen et al., 2024a), Qwen-VL-Chat-9.6B (Bai et al., 2023b), MiniCPM-V 2.6-8B (Yao et al., 2024), Qwen2-VL-7B (Wang et al., 2024), and GLM-4V-9B (Hong et al., 2024). Evaluations are conducted on four benchmarks covering OCR and general question answering: TextVQA (Singh et al., 2019), DocVQA (Mathew et al., 2021), OCRBench (Liu et al., 2023), and MME (Fu et al., 2023), which assesses perception and cognition across 14 subtasks. These MLLMs’ details are in Appendix A.11.

Baselines and Implementation Details. We test W8A8 and W4A8 quantization settings for both visual encoders and LLMs, comparing RTN, SmoothQuant (Xiao et al., 2022), and Quarot (Ashkboos et al., 2024b). Notably, we

Table 3: Comparison of latency and memory saving with Pytorch (BF16), AWQ (W4-only) and ours MQuant (W4A8) on Qwen2-VL-7B. Pytorch and AWQ using the Qwen2-VL-7B official implementation. ↓ means lower values are better, ↑ means larger values are better.

Image size		Latency (s)				Memory (G)				
H × W	Pytorch	AWQ↓	Speedup↑	MQuant↓	Speedup↑	Pytorch	AWQ↓	Improve↑	MQuant↓	Improve↑
840 ²	0.261	0.304 (+0.043)	-14.14%	0.210 (-0.051)	+24.76%	16.45	7.45 (-9.00)	+120.67%	6.50 (-9.95)	+152.92%
1960 ²	1.369	1.598 (+0.229)	-14.26%	1.112 (-0.257)	+16.63%	17.82	8.82 (-9.00)	+100.00%	7.85 (-9.97)	+119.93%
3080 ²	5.208	5.872 (+0.664)	-11.27%	4.488 (-0.720)	+16.02%	20.58	11.58 (-9.00)	+77.60%	10.61 (-9.97)	+96.45%
5600 ²	8.380	9.393 (+1.013)	-10.78%	7.469 (-0.911)	+12.19%	22.22	13.22 (-9.00)	+57.54%	12.25 (-9.97)	+61.65%

Table 4: Multi-Batch speedup comparison of MSQ + AIFS on W4A8 setting. Each row shows the cumulative total of text tokens, images, and textual responses for multi-turn inference.

Batch	Config (Text+Image+Text)			Prefill (s)		Improve↑	Decode (s)		Improve↑	All (s)		Improve↑
	Text	Image	Text	bfp16	MQuant		bfp16	MQuant		bfp16	MQuant	
1	10	2240×2240	50	2.54	1.93	+31.6%	18.01	12.89	+39.7%	20.55	14.82	+38.7%
2	10/10	2240×2240 / 2240×2240	50/100	5.42	4.15	+30.6%	37.82	31.56	+19.8%	43.24	35.71	+21.1%
3	10/10/10	2240×2240 / 2240×2240 / 2240×2240	50/100/150	8.24	6.42	+28.3%	48.03	40.35	+19.0%	56.27	46.77	+20.3%
4	10/10/10/10	2240×2240 / 2240×2240 / 2240×2240 / 2240×2240	50/100/150/200	11.17	8.67	+28.9%	59.09	49.92	+8.4%	70.26	58.59	+20.0%

apply static per-tensor activation quantization for both components, unlike the dynamic per-token quantization typically used in existing MLLMs. The calibration dataset consists of 256 randomly selected samples from the corresponding benchmark training sets (Singh et al., 2019; Mathew et al., 2021; Liu et al., 2023). The batch size for latency is 1.

4.1. Overall Results

Weight-activation quantization results of various MLLMs. MQuant can be applied to the quantization of various MLLMs. As shown in Table 2, our MQuant demonstrates significant improvements over several representative quantization methods. In W8A8 setting, MQuant achieves performance nearly equivalent to that of FP models across all evaluation datasets. Notably, even in the more challenging W4A8 setting, MQuant maintains comparable performance with FP models, while other advanced quantization methods exhibit significant performance degradation. These results indicate that our MQuant provide a general and effective PTQ solution with strong compatibility for maintaining high accuracy in MLLMs under various bits settings.

Table 5: Speedup of MSQ + AIFS on W4A8 setting.

Stage	BF16	Per-token Dyn.	Ours	Ours + GEMV	Speedup
Prefill	1690	1253	1017	-	+23%
Decode	17.5	16.4	13.06	8.2	+100%

4.2. Latency and Memory Analysis

We measure the efficiency of MQuant in terms of speedup and memory usage under varying image resolutions, as well as the decode-stage acceleration introduced by AIFS. Unless otherwise noted, we adopt the common “text-image-text” input format (Duan et al., 2024) with 15 textual tokens, while the image size changes from 280×280 to 5600×5600.

Speedup and Memory Savings. **Overall Speedup** As shown in Table 3, MQuant surpasses PyTorch BF16 and AWQ (W4-only) across all image resolutions, achieving up to **24.76%** speedup over PyTorch at 840 × 840. Even at higher resolutions (e.g., 5600²), MQuant maintains a

12.19% latency improvement, demonstrating scalability. In addition, our method provides memory savings over both PyTorch and AWQ, with reductions exceeding **100%** compared to PyTorch (e.g., **152.92%** at 840²). These benefits primarily arise from (1) eliminating the overhead of token-wise scale computation, and (2) converting mixed tokens into modality-decoupled tokens, avoiding slicing and concatenation when image resolutions become large. **Decode-Stage Acceleration.** We also measure decode time for generating 2,000 tokens with a custom W4A8 GEMV kernel (see Table5). Compared to per-token dynamic quantization, our AIFS+MSQ framework gains **23%** speedup in the prefill stage and **100%** speedup in decode time. By shifting online dynamic quantization to an offline static approach, we greatly reduce inference overhead, for long-sequence tasks. Moreover, since visual tokens are generally pricier than textual ones (Duan et al., 2024), these improvements translate to notable real-world cost reductions (e.g., ≈ 30% for OpenAI-token-based pricing).

Table 6: Latency comparison under multi-turns setting.

Turns	Config in a Turn			All(s)		Improve ↑
	Text	Image	Text	bfp16	Ours	
1	10	2240x2240	50	20.55	14.82	+38.7%
2	10	2240x2240	50	44.06	32.61	+35.1%
3	10	2240x2240	50	76.67	59.48	+28.9%

Acceleration for Multi-batch and Multi-turn Inference.

For multi-batch scenarios, we employ a “text-image-text” input setting at 2240×2240 resolution, with each batch containing text lengths varying from 50 to 200, and uniformly generating 512 tokens during decoding. We use left-padding (pad_token_id) to align sequences of different lengths, masking out the padded regions to ensure they do not affect attention computations (Figure A.4 provides a schematic). Notably, our AIFS procedure remains fully compatible with multi-batch inputs, requiring no additional overhead. As shown in Table 4, MQuant consistently achieves around 20% faster inference across both prefill

Table 7: The accuracy and speedup of our MSQ and AIFS scheme on the linear layer during prefill stage. The input sequence is structured as "text-image-text-image-text-image-text" with an image resolution of 2240 × 2240 and 50 textual tokens. Latency were tested on an NVIDIA RTX 6000 Ada Generation.

Activation	Weight	T.VQA↑	D.VQA↑	OCRB.↑	MME↑	Latency ↓ (s)	Speedup ↑
BF16	BF16	84.43	93.87	842	2319	1.690	-
W4-g128(AWQ)	BF16	83.93 (-0.50)	93.13 (-0.74)	828 (-14)	2252 (-67)	2.057 (+0.367)	-17.8%
A8-per-token dyn	W4-per-channel sta	84.32 (-0.11)	93.61 (-0.26)	830 (-12)	2269 (-50)	1.253 (-0.437)	+34.9%
A8-per-tensor sta		40.20 (-44.12)	38.82 (-54.79)	422 (-408)	1082 (-1187)	1.016 (-0.674)	+66.3%
A8-MSQ		84.32 (-0.11)	93.61 (-0.26)	830 (-12)	2269 (-50)	1.085 (-0.605)	+55.8%
A8-MSQ+AIFS		84.32 (-0.11)	93.61 (-0.26)	830 (-12)	2269 (-50)	1.017 (-0.673)	+66.2%

and decode stages compared to the floating-point baseline when the batch size ranges from 1 to 4. **For multi-turn dialogue**, we retain the same "text-image-text" format and resolution, with each turn containing 50 text tokens and a uniform decode length of 512 tokens. By maintaining key-value caches and position IDs across turns, we preserve context during the dialogue. As Table 6 shows, MQuant reduces end-to-end inference time by up to 38.7% over the floating-point baseline for 1–3 turns, showing the efficiency of our quantization approach in multi-turn settings.

4.3. Ablation Study

In this section, we select Qwen2-VL-7B (Wang et al., 2024), currently one of the most powerful open-source MLLMs, to ablate the effectiveness of our proposed designs.

Table 8: Ablation study of proposed quantization designs on Qwen2-VL-7B (Wang et al., 2024) with W4A8 setting.

Methods			T.VQA↑	D.VQA↑	OCRB.↑	MME↑	Lat (ms) ↓
Static	AIFS + MSQ	RMS					
BF16			84.43	93.87	842	2319	6523
✓	✗	✗	71.44	83.96	670	1911	5479
✓	✓	✗	78.95	87.55	721	2095	5484
✓	✓	✓	84.32	93.58	824	2255	5471

Ablation Study of Proposed Quantization Methods. We perform ablations on Qwen2-VL-7B (Table 8) to isolate the contributions of each quantization component. Beginning with a baseline that applies GPTQ plus Hadamard transformations to both the LLM and vision parts, we progressively introduce MSQ and AIFS for the LLM. This significantly boosts accuracy, highlighting their effectiveness on text tokens. Next, leveraging offline and online Hadamard rotations in the vision encoder further improves results. Finally, incorporating RMS to suppress newly arising outliers achieves near-floating-point performance, underscoring the overall robustness and efficiency of our pipeline.

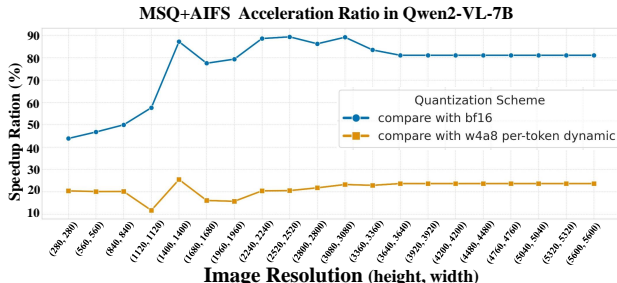


Figure 5: The Speedup of AIFS+MSQ on Qwen2-VL-7B.

Accuracy & Speedup via AIFS. While MSQ addresses the modality discrepancy, AIFS further reorders visual and textual tokens into a unified sequence to enable efficient per-tensor static quantization of activations. Table 7 shows that MSQ+AIFS not only achieves the same speedup as naïve per-tensor static quantization but also maintains near-floating-point accuracy across linear layers. Figure 5 further illustrates that AIFS yields speedups of 20%–80% as resolution increases, corroborating that rearranging tokens avoids the high overhead of dynamic per-token quantization.

Table 9: Comparative quantized results under different quantization settings on Qwen2-VL-7B (Wang et al., 2024). † means re-implementation based on the official weight-only quantization setting with a group size of 128.

Method	Bits Setting		T.VQA↑	D.VQA↑	OCRB.↑	MME↑
	Visual	LLM				
-	BF16	BF16	84.43	93.87	842	2319
GPTQ (g128)†	BF16	W8	84.33	93.97	842	2313
GPTQ (g128)†	BF16	W4	84.18	93.25	831	2285
AWQ (g128)†	BF16	W4	83.93	93.13	828	2252
MQuant (g128)	BF16	W4	84.55	93.18	832	2304
MQuant (g128)	W4	W4	84.70	93.57	828	2292
MQuant	W4A8	W4A8	84.32	93.58	824	2255

Weight-only Quantization. We compare our weight-only quantization results with the official Qwen2-VL-7B, which uses GPTQ (Frantar et al., 2022) and AWQ (Lin et al., 2023) to quantize only the LLM while keeping the visual encoder in BF16. For fairness, we adopt the same group size of 128. As shown in Table 6, our W4 LLM quantization aligns with their settings, achieving nearly lossless accuracy compared to other methods. Extending W4 quantization to the visual encoder enables 4-bit quantization of the entire MLLM; MQuant still performs comparably to the BF16 model and even surpasses other methods. Under the W4A8 weight-activation quantization setting, our results remain consistent, with some metrics surpassing advanced weight-only methods. These experiments confirm MQuant’s effectiveness and robustness across various quantization configurations, whether for weight-only or weight-activation quantization, and for partial or full quantization of MLLMs.

5. Conclusion

In this paper, we propose MQuant, an accurate and efficient post-training quantization (PTQ) framework specifically designed for MLLMs. Our approach addresses the unique chal-

allenges of MLLMs by applying **Modality-Specific Static Quantization (MSQ)** to handle distribution mismatches between vision and text tokens, and introducing an **Attention-Invariant Flexible Switching (AIFS)** mechanism to reduce time-to-first-token (TTFT) with static per-tensor scaling. Furthermore, we reveal that online Hadamard rotations can introduce severe weight outliers, and propose **Rotation Magnitude Suppression (RMS)** to effectively mitigate this issue. Extensive experiments on five mainstream MLLMs demonstrate that *MQuant* achieves near-floating-point accuracy under the W4A8 setting, highlighting its potential to advance MLLMs quantization and facilitate practical deployment in resource-constrained environments.

References

- Achiam, J., Adler, S., Agarwal, S., Ahmad, L., Akkaya, I., Aleman, F. L., Almeida, D., Altenschmidt, J., Altman, S., Anadkat, S., et al. Gpt-4 technical report. *arXiv preprint arXiv:2303.08774*, 2023a.
- Achiam, J., Adler, S., Agarwal, S., Ahmad, L., Akkaya, I., Aleman, F. L., Almeida, D., Altenschmidt, J., Altman, S., Anadkat, S., et al. GPT-4 technical report. *arXiv preprint arXiv:2303.08774*, 2023b.
- Alayrac, J.-B., Donahue, J., Luc, P., Miech, A., Barr, I., Hasson, Y., Lenc, K., Mensch, A., Millican, K., Reynolds, M., et al. Flamingo: A visual language model for few-shot learning. *NeurIPS*, 35:23716–23736, 2022.
- Ashkboos, S., Croci, M. L., Nascimento, M. G. d., Hoefler, T., and Hensman, J. SliceGPT: Compress large language models by deleting rows and columns. *International Conference on Learning Representations (ICLR)*, 2024a.
- Ashkboos, S., Mohtashami, A., Croci, M. L., Li, B., Jaggi, M., Alistarh, D., Hoefler, T., and Hensman, J. Quarot: Outlier-free 4-bit inference in rotated llms. *arXiv preprint arXiv:2404.00456*, 2024b.
- Ba, J. Layer normalization. *arXiv preprint arXiv:1607.06450*, 2016.
- Bai, J., Bai, S., Chu, Y., Cui, Z., et al. Qwen technical report. *arXiv preprint arXiv:2309.16609*, 2023a.
- Bai, J., Bai, S., Yang, S., Wang, S., Tan, S., Wang, P., Lin, J., Zhou, C., and Zhou, J. Qwen-vl: A frontier large vision-language model with versatile abilities. *arXiv preprint arXiv:2308.12966*, 2023b.
- Brown, T., Mann, B., Ryder, N., Subbiah, M., Kaplan, J. D., Dhariwal, P., Neelakantan, A., Shyam, P., Sastry, G., Askell, A., et al. Language models are few-shot learners. *Advances in Neural Information Processing Systems*, 2020.
- Cai, Z., Cao, M., Chen, H., Chen, K., et al. Internlm2 technical report, 2024.
- Chee, J., Cai, Y., Kuleshov, V., and De Sa, C. M. Quip: 2-bit quantization of large language models with guarantees. *Advances in Neural Information Processing Systems*, 36, 2024.
- Chen, Z., Wang, W., Tian, H., Ye, S., Gao, Z., Cui, E., Tong, W., Hu, K., Luo, J., Ma, Z., et al. How far are we to gpt-4v? closing the gap to commercial multimodal models with open-source suites. *arXiv preprint arXiv:2404.16821*, 2024a.
- Chen, Z., Wu, J., Wang, W., Su, W., Chen, G., Xing, S., Zhong, M., Zhang, Q., Zhu, X., Lu, L., et al. Internvl: Scaling up vision foundation models and aligning for generic visual-linguistic tasks. In *Proceedings of the IEEE/CVF Conference on Computer Vision and Pattern Recognition*, pp. 24185–24198, 2024b.
- Chu, X., Qiao, L., Zhang, X., Xu, S., Wei, F., Yang, Y., Sun, X., Hu, Y., Lin, X., Zhang, B., et al. Mobilevlm v2: Faster and stronger baseline for vision language model. *arXiv preprint arXiv:2402.03766*, 2024.
- Dao, T., Fu, D., Ermon, S., Rudra, A., and Ré, C. Flashattention: Fast and memory-efficient exact attention with io-awareness. *Advances in Neural Information Processing Systems*, 35:16344–16359, 2022.
- Dosovitskiy, A. An image is worth 16x16 words: Transformers for image recognition at scale. *ICLR*, 2021.
- Duan, H., Yang, J., Qiao, Y., Fang, X., Chen, L., Liu, Y., Dong, X., Zang, Y., Zhang, P., Wang, J., et al. Vlmevalkit: An open-source toolkit for evaluating large multi-modality models. In *Proceedings of the 32nd ACM International Conference on Multimedia*, pp. 11198–11201, 2024.
- Dubey, A., Jauhri, A., Pandey, A., Kadian, A., Al-Dahle, A., Letman, A., Mathur, A., Schelten, A., Yang, A., Fan, A., et al. The llama 3 herd of models. *arXiv preprint arXiv:2407.21783*, 2024.
- Frantar, E., Ashkboos, S., Hoefler, T., and Alistarh, D. GPTQ: Accurate post-training quantization for generative pre-trained transformers. *arXiv preprint arXiv:2210.17323*, 2022.
- Fu, C., Chen, P., Shen, Y., Qin, Y., Zhang, M., Lin, X., Yang, J., Zheng, X., Li, K., Sun, X., Wu, Y., and Ji, R. MME: A comprehensive evaluation benchmark for multimodal large language models. *arXiv preprint arXiv:2306.13394*, 2023.

- GLM, T., Zeng, A., Xu, B., Wang, B., Zhang, C., Yin, D., Rojas, D., Feng, G., Zhao, H., Lai, H., et al. Chatglm: A family of large language models from glm-130b to glm-4 all tools. *arXiv preprint arXiv:2406.12793*, 2024.
- Hong, W., Wang, W., Ding, M., Yu, W., Lv, Q., Wang, Y., Cheng, Y., Huang, S., Ji, J., Xue, Z., et al. Cogvlm2: Visual language models for image and video understanding. *arXiv preprint arXiv:2408.16500*, 2024.
- Hu, S., Tu, Y., Han, X., He, C., Cui, G., Long, X., Zheng, Z., Fang, Y., Huang, Y., Zhao, W., et al. MiniCPM: Unveiling the potential of small language models with scalable training strategies. *arXiv preprint arXiv:2404.06395*, 2024a.
- Hu, X., Chen, Y., Yang, D., Zhou, S., Yuan, Z., Yu, J., and Xu, C. I-llm: Efficient integer-only inference for fully-quantized low-bit large language models. *arXiv preprint arXiv:2405.17849*, 2024b.
- Hu, X., Cheng, Y., Yang, D., Xu, Z., Yuan, Z., Yu, J., Xu, C., Jiang, Z., and Zhou, S. Ostquant: Refining large language model quantization with orthogonal and scaling transformations for better distribution fitting. *arXiv preprint arXiv:2501.13987*, 2025.
- Huang, S., Dong, L., Wang, W., Hao, Y., Singhal, S., Ma, S., Lv, T., Cui, L., Mohammed, O. K., Patra, B., et al. Language is not all you need: Aligning perception with language models. *NeurIPS*, 36, 2024.
- Ilharco, G., Wortsman, M., Wightman, R., Gordon, C., Carlini, N., Taori, R., Dave, A., Shankar, V., Namkoong, H., Miller, J., Hajishirzi, H., Farhadi, A., and Schmidt, L. Openclip, July 2021. URL <https://doi.org/10.5281/zenodo.5143773>. If you use this software, please cite it as below.
- Li, J., Li, D., Savarese, S., and Hoi, S. BLIP-2: Bootstrapping language-image pre-training with frozen image encoders and large language models. *ICML*, pp. 19730–19742, 2023.
- Li, Y., Zhang, Y., Wang, C., Zhong, Z., Chen, Y., Chu, R., Liu, S., and Jia, J. Mini-Gemini: Mining the potential of multi-modality vision language models. *arXiv preprint arXiv:2403.18814*, 2024.
- Lin, J., Tang, J., Tang, H., Yang, S., Dang, X., and Han, S. Awq: Activation-aware weight quantization for llm compression and acceleration. *arXiv preprint arXiv:2306.00978*, 2023.
- Liu, H., Li, C., Wu, Q., and Lee, Y. J. Visual instruction tuning. *NeurIPS*, 36, 2024.
- Liu, Y., Li, Z., Li, H., Yu, W., Huang, M., Peng, D., Liu, M., Chen, M., Li, C., Jin, L., et al. On the hidden mystery of OCR in large multimodal models. *arXiv preprint arXiv:2305.07895*, 2023.
- Mathew, M., Karatzas, D., and Jawahar, C. DocVQA: A dataset for VQA on document images. In *WACV*, pp. 2200–2209, 2021.
- Radford, A., Kim, J. W., Hallacy, C., Ramesh, A., Goh, G., Agarwal, S., Sastry, G., Askell, A., Mishkin, P., Clark, J., et al. Learning transferable visual models from natural language supervision. In *ICML*, pp. 8748–8763. PMLR, 2021.
- Reid, M., Savinov, N., Teplyashin, D., Lepikhin, D., Lillcrap, T., Alayrac, J.-b., Soricut, R., Lazaridou, A., Firat, O., Schrittwieser, J., et al. Gemini 1.5: Unlocking multimodal understanding across millions of tokens of context. *arXiv preprint arXiv:2403.05530*, 2024.
- Shang, Y., Yuan, Z., Wu, Q., and Dong, Z. Pb-llm: Partially binarized large language models. *arXiv preprint arXiv:2310.00034*, 2023.
- Shao, W., Chen, M., Zhang, Z., Xu, P., Zhao, L., Li, Z., Zhang, K., Gao, P., Qiao, Y., and Luo, P. Omniquant: Omnidirectionally calibrated quantization for large language models. *CoRR*, abs/2308.13137, 2023.
- Singh, A., Natarajan, V., Shah, M., Jiang, Y., Chen, X., Batra, D., Parikh, D., and Rohrbach, M. Towards VQA models that can read. In *CVPR*, pp. 8317–8326, 2019.
- Su, J., Lu, Y., Pan, S., Wen, B., and Liu, Y. Roformer: Enhanced transformer with rotary position embedding, 2021.
- Tan, F., Lee, R., Łukasz Dudziak, Hu, S. X., Bhattacharya, S., Hospedales, T., Tzimiropoulos, G., and Martinezs, B. Mobilequant: Mobile-friendly quantization for on-device language models. In *The 2024 Conference on Empirical Methods in Natural Language Processing*, 2024. URL <https://openreview.net/forum?id=48ptWWA54E>.
- Touvron, H., Lavril, T., Izacard, G., Martinet, X., Lachaux, M.-A., Lacroix, T., Rozière, B., Goyal, N., Hambro, E., Azhar, F., et al. Llama: Open and efficient foundation language models. *arXiv preprint arXiv:2302.13971*, 2023a.
- Touvron, H., Martin, L., Stone, K., Albert, P., Almahairi, A., Babaei, Y., Bashlykov, N., Batra, S., Bhargava, P., Bhosale, S., et al. Llama 2: Open foundation and fine-tuned chat models. *arXiv preprint arXiv:2307.09288*, 2023b.

- Tseng, A., Chee, J., Sun, Q., Kuleshov, V., and De Sa, C. Quip#: Even better llm quantization with hadamard incoherence and lattice codebooks. *Forty-first International Conference on Machine Learning*, 2024.
- Vaswani, A., Shazeer, N., Parmar, N., Uszkoreit, J., Jones, L., Gomez, A. N., Kaiser, Ł., and Polosukhin, I. Attention is all you need. *Advances in neural information processing systems*, 2017.
- Wang, P., Bai, S., Tan, S., Wang, S., Fan, Z., Bai, J., Chen, K., Liu, X., Wang, J., Ge, W., Fan, Y., Dang, K., Du, M., Ren, X., Men, R., Liu, D., Zhou, C., Zhou, J., and Lin, J. Qwen2-vl: Enhancing vision-language model’s perception of the world at any resolution. *arXiv preprint arXiv:2409.12191*, 2024.
- Wang, W., Lv, Q., Yu, W., Hong, W., Qi, J., Wang, Y., Ji, J., Yang, Z., Zhao, L., Song, X., et al. CogVLM: Visual expert for pretrained language models. *arXiv preprint arXiv:2311.03079*, 2023.
- Wei, X., Zhang, Y., Zhang, X., Gong, R., Zhang, S., Zhang, Q., Yu, F., and Liu, X. Outlier suppression: Pushing the limit of low-bit transformer language models. *Advances in Neural Information Processing Systems*, 2022.
- Xiao, G., Lin, J., Seznec, M., Demouth, J., and Han, S. Smoothquant: Accurate and efficient post-training quantization for large language models. *arXiv preprint arXiv:2211.10438*, 2022.
- Yao, Y., Yu, T., Zhang, A., Wang, C., Cui, J., Zhu, H., Cai, T., Li, H., Zhao, W., He, Z., et al. Minicpm-v: A gpt-4v level mllm on your phone. *arXiv preprint arXiv:2408.01800*, 2024.
- Yao, Z., Aminabadi, R. Y., Zhang, M., Wu, X., Li, C., and He, Y. Zeroquant: Efficient and affordable post-training quantization for large-scale transformers. *arXiv preprint arXiv:2206.01861*, 2022.
- Yuan, Z., Niu, L., Liu, J., Liu, W., Wang, X., Shang, Y., Sun, G., Wu, Q., Wu, J., and Wu, B. Rptq: Reorder-based post-training quantization for large language models. *arXiv preprint arXiv:2304.01089*, 2023a.
- Yuan, Z., Shang, Y., Song, Y., Wu, Q., Yan, Y., and Sun, G. Asvd: Activation-aware singular value decomposition for compressing large language models. *arXiv preprint arXiv:2312.05821*, 2023b.
- Yuan, Z., Shang, Y., Zhou, Y., Dong, Z., Xue, C., Wu, B., Li, Z., Gu, Q., Lee, Y. J., Yan, Y., et al. Llm inference unveiled: Survey and roofline model insights. *arXiv preprint arXiv:2402.16363*, 2024.
- Yue, Y., Yuan, Z., Duanmu, H., Zhou, S., Wu, J., and Nie, L. Wkvquant: Quantizing weight and key/value cache for large language models gains more. 2024.
- Zhang, B. et al. Root mean square layer normalization. *Advances in Neural Information Processing Systems*, 32, 2019.
- Zhang, Y., Zhang, P., Huang, M., Xiang, J., Wang, Y., Wang, C., Zhang, Y., Yu, L., Liu, C., and Lin, W. Qqq: Quality quattuor-bit quantization for large language models. *arXiv preprint arXiv:2406.09904*, 2024.
- Zhao, W. X., Zhou, K., Li, J., Tang, T., Wang, X., Hou, Y., Min, Y., Zhang, B., Zhang, J., Dong, Z., et al. A survey of large language models. *arXiv preprint arXiv:2303.18223*, 2023.
- Zheng, L., Chiang, W.-L., Sheng, Y., Zhuang, S., Wu, Z., Zhuang, Y., Lin, Z., Li, Z., Li, D., Xing, E., et al. Judging LLM-as-a-judge with MT-Bench and Chatbot Arena. *NeurIPS*, 36, 2024.
- Zhu, D., Chen, J., Shen, X., Li, X., and Elhoseiny, M. MiniGPT-4: Enhancing vision-language understanding with advanced large language models. *arXiv preprint arXiv:2304.10592*, 2023.

A. Appendix

A.1. MQuant Algorithm

Here, we present our *MQuant* algorithm for MLLMs in Algorithm 1.

Algorithm 1 *MQuant* Quantization Algorithm

Input: Full-precision (FP) MLLM model with a vision encoder E , visual-language projector P , and a large language model **LLM**; Calibration dataset D^c .

Output:

- For E and P : per-channel weight scale s_w^E , per-channel weight zero-point z_w^E , per-tensor activation scales s_a^E , per-tensor activation zero-point z_a^E .
 - For **LLM**: per-channel weight scale s_w^{llm} , per-channel weight zero-point z_w^{llm} , per-tensor activation scales s_a^{llm} for visual tokens and s_a^{llm} for textual tokens, per-tensor activation zero-points z_a^{llm} for visual tokens and z_a^{llm} for textual tokens.
- 1: Apply Hadamard Rotation to the LLM Part as described:
 - 2: Apply the offline and online Hadamard rotations to all the weights and activations in **LLM**.
 - 3: Quantize Weights of the LLM:
 - 4: Input the calibration dataset D^c to the FP MLLM.
 - 5: Use GPTQ to quantize the weights for **LLM**, obtaining per-channel weight quantization parameters s_w^{llm} and z_w^{llm} .
 - 6: For the LLM Part:
 - (a) Input D^c to the FP MLLM.
 - (b) Compute per-tensor activation quantization parameters s_a^{llm} and s_a^{llm} , z_a^{llm} and z_a^{llm} for visual and textual tokens respectively, based on the proposed Modality-Specific Static Quantization (MSQ) in Sec 3.1.
 - (c) Reorder the input mixed token sequence from $E = e_1^t, \dots, e_m^v, \dots, e_n^v, \dots, e_L^t$ to a unified modality-decoupled sequence $E^u = e_m^v, \dots, e_n^v, e_1^t, \dots, e_{m-1}^t, \dots, e_{n+1}^t, \dots, e_L^t$ using the proposed Attention-Invariant Flexible Switching (AIFS) scheme in Sec 3.1.
 - 7: Transform all the LayerNorm to RMSNorm in MLLM vision encoder E and Visual-Language Projector P using the proposed Post LayerNorm-to-RMSNorm transformation in Sec 3.2.
 - 8: Apply the offline and online Hadamard rotations to all the weights and activations in E and P .
 - 9: Quantize Weights of E and P :
 - 10: Input D^c to the transformed FP vision encoder E and Visual-Language Projector P .
 - 11: Use GPTQ to quantize E and P , obtaining per-channel weight quantization parameters s_w^E and z_w^E .
 - 12: Address the weight outliers using caused by online Hadamard based on the proposed Rotation Magnitude Suppression (RMS) in Sec 3.2.
-

A.2. Rotary Position Embedding for Attention-Invariant Flexible Switching

Many modern LLMs (Touvron et al., 2023a;b; Dubey et al., 2024) use rotary position embedding (RoPE) (Su et al., 2021) to encode information about the order of tokens in the input sequence. Rotary position embeddings are linear transformations applied to keys and queries defined as:

$$R_{\Theta, m}^{d_h} = \begin{pmatrix} \cos i\theta_1 & -\sin i\theta_1 & 0 & 0 & \cdots & 0 & 0 \\ \sin i\theta_1 & \cos i\theta_1 & 0 & 0 & \cdots & 0 & 0 \\ 0 & 0 & \cos i\theta_2 & -\sin i\theta_2 & \cdots & 0 & 0 \\ 0 & 0 & \sin i\theta_2 & \cos i\theta_2 & \cdots & 0 & 0 \\ \vdots & \vdots & \vdots & \vdots & \ddots & \vdots & \vdots \\ 0 & 0 & 0 & 0 & \cdots & \cos i\theta_{d_h/2} & -\sin i\theta_{d_h/2} \\ 0 & 0 & 0 & 0 & \cdots & \sin i\theta_{d_h/2} & \cos i\theta_{d_h/2} \end{pmatrix} \quad (9)$$

where $i \in [1, L]$ is the token index, $\Theta = \{\theta_i = 10000^{-2(i-1)/D}, i \in [1, 2, \dots, D/2]\}$, and $\theta_i, i \in 1..D/2$ are predefined constants.

In the proposed Attention-Invariant Flexible Switching (AIFS) mechanism, we also apply the rearrangement for position embedding to maintain the computation equivalence. For a mixed input token $E = \{e_1^t, \dots, e_m^v, \dots, e_n^v, \dots, e_L^t\} \in (\mathbf{E}_v, \mathbf{E}_t)$ (in Eq 3), where m and n denote the start and end indices of the visual tokens. Specifically, after AIFS, the unified token can be formulated as: $E = \{e_m^v, \dots, e_n^v, e_1^t, \dots, e_{m-1}^t, \dots, e_L^t\} \in (\mathbf{E}_v, \mathbf{E}_t)$. Therefore, the unified token indices after AIFS can be represented as:

$$(m, \dots, n, 1, \dots, m-1, n+1, \dots, L) = AIFS(1, \dots, m, \dots, n, \dots, L) \quad (10)$$

Due to we are aware of the final indices for input token after AIFS, than we can utilize the reorder token indices for Eq 9 to get the corresponding position embedding.

A.3. Weights Outliers after Online Hadamard Transformation

Following (Tseng et al., 2024; Ashkboos et al., 2024b) we make use of fast Hadamard transformation where convenient. Hadamard matrix is an orthogonal matrix with entries proportional to $\{+1, -1\}$. A Walsh-Hadamard matrix is a square matrix of size 2^n with For a Hadamard matrix:

$$\mathbf{H}_2 = \frac{1}{\sqrt{2}} \begin{bmatrix} 1 & 1 \\ 1 & -1 \end{bmatrix} \quad \text{and} \quad \mathbf{H}_{2^n} = \mathbf{H}_2 \otimes \mathbf{H}_{2^{n-1}}. \quad (11)$$

$$(\mathbf{AB})_{ij} = \sum_{r=1}^n a_{ir} b_{rj} = a_{i1} b_{1j} + a_{i2} b_{2j} + \dots + a_{in} b_{nj} \quad (12)$$

Thereby the \mathbf{HW}_{ℓ_2} can be formulated as:

$$(\mathbf{HW}_{\ell_2})_{ij} = \sum_{r=1}^n h_{ir} w_{rj} = h_{i1} w_{1j} + h_{i2} w_{2j} + \dots + h_{in} w_{nj} \quad (13)$$

where $\mathbf{H} \in \mathbb{R}^{d_{in} \times d_{in}}$ and $\mathbf{W}_{\ell_2} \in \mathbb{R}^{d_{in} \times d_{out}}$, d_{in} and d_{out} is the dimension of input and output of weight \mathbf{W}_{ℓ_2} . Due to the properties of the Hadamard matrix \mathbf{H} , whose first row consists entirely of 1, for the first row in (\mathbf{HW}_{ℓ_2}) , $(\mathbf{HW}_{\ell_2})_{0j} = \sum_{r=1}^n w_{rj}$, due to the property of Hadamard matrix \mathbf{H} . So, the values in \mathbf{W}_{ℓ_2} are subject to continuous accumulation and summation, resulting in the exists of outliers in the first row of the output matrix \mathbf{HW}_{ℓ_2} . Notably, the matrix $\mathbf{HW}_{\ell_2} \mathbf{Q}$ still has the same problem, for simplicity, we omit the matrix \mathbf{Q} in the main paper.

A.4. Attention Mask in AIFS when Multi-batch Inference.

During multi-batch inference, we first identify the longest token length within the batch. Subsequently, we left-pad the shorter sequences with *padding* to align all batches to this maximum length. By applying left padding, the padding tokens are associated with the image modality. Additionally, the padded regions are assigned a mask value of 0, ensuring that they do not interfere with attention computations and thereby do not affect the final results. For clarity, we also plot an illustration of causal mask when batch size > 1 .

A.5. Effectiveness of Rotational Magnitude Suppression for Weight Outliers in LLMs.

For LLMs, compared to the original Quarot, integrating RMS with Quarot leads to performance improvements across LLaMA2 models with 7B, 13B, and 70B parameters, as detailed in Table 10. For MLLMs, ablation studies presented in Table 8 demonstrate that the RMS method significantly enhances quantization performance.

A.6. Image Tokens in Various MLLMs

As shown in Fig 7, for different MLLMs (Bai et al., 2023b; Wang et al., 2024; Yao et al., 2024; Chen et al., 2024b), the number of prefill visual tokens grows

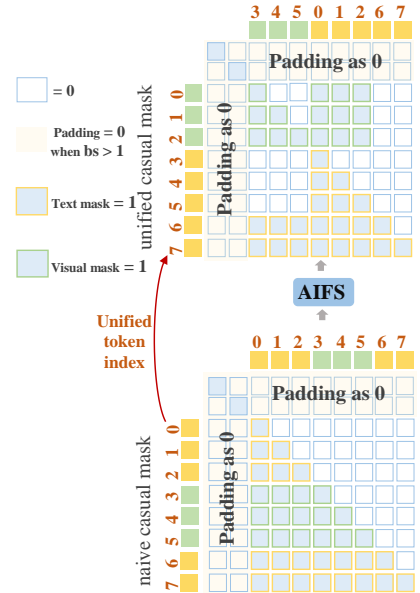


Figure 6: The illustration of causal mask when batch size > 1 .

Table 10: WikiText-2 perplexity (PPL) on 4-bit quantized LLaMA2 models with an input sequence length of 2048. Lower PPL is better.

Method	Weight Quantization	PPL		
		LLaMA2 7B	LLaMA2 13B	LLaMA2 70B
Baseline	–	5.47	4.88	3.32
QuaRot	GPTQ	6.10	5.40	3.79
QuaRot + RMS	GPTQ	6.04	5.32	3.67

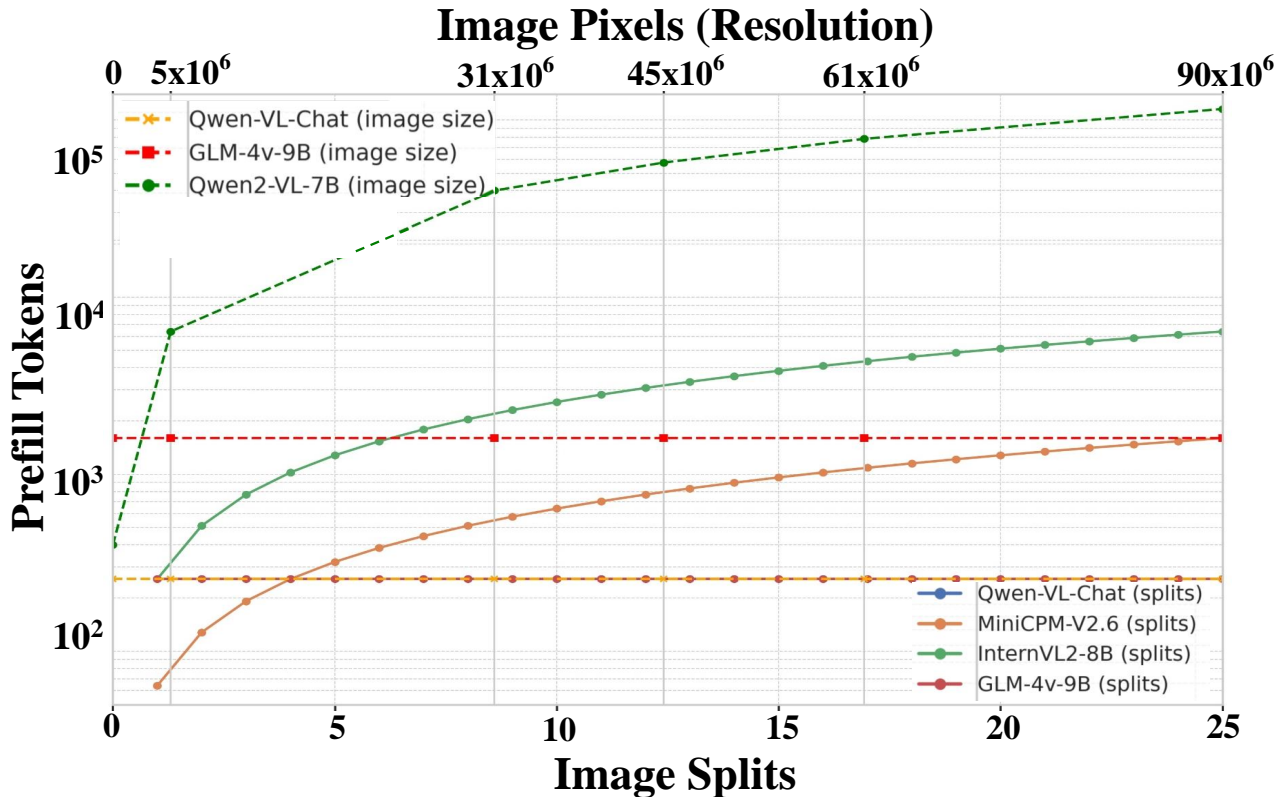


Figure 7: The number of prefill visual tokens across different MLLMs as the image splits or resolution increases.

as image resolution increases. This rapid expansion in token count exacerbates the inference latency, particularly in per-token dynamic quantization, which requires separate processing for each token, such as memory access and scale computation. As a result, the TTFT in MLLMs increases drastically, severely impacting overall inference latency. Moreover, in higher-demand scenarios such as video-based tasks and multi-image dialogues, the accumulation of visual tokens becomes even more pronounced, further exacerbating the increase in TTFT.

A.7. RMS Algorithm

Here, we present the algorithm of our *RMS* design with Quarot in Algorithm 2.

A.8. Speedup and Memory Savings with Scaling Image Resolution

We fixed the input sequence as "text-image-text" with 15 textual tokens and present the detailed changes of speed and memory, varying the image resolution from 280×280 to 5600×5600 . Notably, the "text-image-text" sequence setting is not arbitrarily chosen; instead, it is a common setting in existing evaluation datasets (Duan et al., 2024). We evaluate

Algorithm 2 RMS Integration with Quarot

```

Require: An LLM or MLLM model
Ensure: Quantized model with RMS
1: Initialize an empty list marks
2: for each linear layer in the model do
3:   if Layer satisfies Equation 8 then
4:     Mark the layer and append its ID to marks
5:   end if
6: end for
7: Apply Quarot or other Hadamard-based transformations to the model
8: for each layer ID in marks do
9:   Modify the layer’s implementation using the RMS method
10: end for
11: Quantize the model
12: return model

```

Table 11: Comparison of latency and memory saving with Pytorch and AWQ on Qwen2-VL-7B. ‡ means the Qwen2-VL-7B official implementation.

Image size H × W	Pytorch‡ (BF16)		AWQ‡ (W4-only)		MQuant (W4A8)	
	Latency(s)	Memory(G)	Latency(s)	Memory(G)	Latency(s)	Memory(G)
280 ²	0.257	16.45	0.286 (-10.14%)	7.45 (+120.67%)	0.220 (+16.82%)	6.50 (+152.92%)
560 ²	0.252	16.45	0.292 (-13.70%)	7.45 (+120.67%)	0.211 (+19.48%)	6.50 (+152.92%)
840 ²	0.261	16.45	0.304 (-14.14%)	7.45 (+120.67%)	0.210 (+24.76%)	6.50 (+152.92%)
1120 ²	0.326	16.58	0.384 (-15.10%)	7.56 (+119.51%)	0.262 (+24.48%)	6.61 (+151.59%)
1400 ²	0.559	16.90	0.652 (-14.29%)	7.90 (+113.92%)	0.432 (+20.24%)	6.97 (+142.71%)
1680 ²	0.881	17.33	1.066 (-17.39%)	8.33 (+108.57%)	0.705 (+18.23%)	7.40 (+130.27%)
1960 ²	1.369	17.82	1.598 (-14.26%)	8.82 (+100.00%)	1.112 (+16.63%)	7.85 (+119.93%)
2240 ²	2.013	18.40	2.294 (-12.24%)	9.40 (+95.74%)	1.653 (+17.83%)	8.44 (+117.84%)
2520 ²	2.820	19.04	3.175 (-11.14%)	10.05 (+89.59%)	2.357 (+19.63%)	9.10 (+109.92%)
2880 ²	3.883	19.77	4.345 (-10.64%)	10.77 (+83.81%)	3.297 (+17.69%)	9.82 (+101.07%)
3080 ²	5.208	20.58	5.872 (-11.27%)	11.58 (+77.60%)	4.488 (+16.02%)	10.61 (+96.45%)
3360 ²	6.814	21.46	7.548 (-9.73%)	12.46 (+70.65%)	6.004 (+13.41%)	11.50 (+83.01%)
3640 ²	8.360	22.22	9.377 (-10.84%)	13.22 (+57.54%)	7.469 (+11.91%)	12.25 (+61.65%)
4480 ²	8.349	22.22	9.379 (-10.97%)	13.22 (+57.54%)	7.469 (+11.71%)	12.25 (+61.65%)
5600 ²	8.380	22.22	9.393 (-10.78%)	13.22 (+57.54%)	7.469 (+12.19%)	12.25 (+61.65%)

speedup and memory savings by comparing PyTorch’s BF16, AWQ (W4-only), and our MQuant (W4A8). **Speedup:** As shown in Table 11, MQuant consistently achieves speedups over both PyTorch and AWQ across all resolutions, with a maximum of 24.76% over PyTorch at 840 × 840. Notably, MQuant outperforms AWQ, which is slower than PyTorch at most resolutions due to negative speedups. This significant speedup highlights the advantage of our per-tensor static quantization, eliminating the overhead of token-wise scale computation. Even at higher resolutions (e.g., 5600²), MQuant maintains a 12.19% latency improvement, demonstrating scalability across various image sizes. **Memory Savings:** MQuant offers substantial memory reductions compared to both PyTorch and AWQ. It consistently reduces memory usage by over 100% compared to PyTorch (e.g., 152.92% at 840²) and significantly outperforms AWQ’s memory efficiency, achieving up to 101.07% savings at higher resolutions. These experiments demonstrate MQuant’s strengths in both latency and memory savings, achieving up to 24.76% faster inference and reducing memory consumption by over 100% compared to baseline methods. This makes MQuant a more efficient solution for deploying MLLMs in resource-constrained environments.

A.9. Comparison of Online vs. Without Online Hadamard Transform in Quarot

In this section, we evaluate how online Hadamard transformations affect perplexity (PPL) in Quarot for different LLaMA2 models (7B and 13B) under two bit settings, W4A8KV4 and W4A4KV4. As shown in Table 12, enabling online Hadamard transforms yields consistent improvements, especially under more aggressive quantization (e.g., W4A4KV4).

We observe that online Hadamard transforms provide substantial gains when using W4A4KV4 for both 7B and 13B models,

Table 12: Comparison of perplexity (PPL) with or without online Hadamard transforms in Quorot, evaluated on LLaMA2 models of sizes 7B and 13B. Lower PPL is better.

Model	Bit Setting	PPL	
		With Online	Without Online
LLaMA2 7B	W4A8KV4	5.736	5.830
LLaMA2 7B	W4A4KV4	6.358	14.375
LLaMA2 13B	W4A8KV4	5.123	5.146
LLaMA2 13B	W4A4KV4	5.585	24.401

reducing PPL from over 14.3 to 6.36 (7B) and from 24.4 to 5.58 (13B), respectively. These results demonstrate the effectiveness of online Hadamard transformations in maintaining quantization accuracy at lower bit precision.

A.10. Advantage of Proposed MSQ and AIFS

In per-tensor static quantization, the quantization parameters (i.e., scale and zero-point) are precomputed for an entire tensor (e.g., weights or activations) and remain fixed throughout inference. While efficient, this approach often leads to large and unacceptable accuracy loss in MLLMs due to their diverse activation distributions across varying inputs.

In contrast, per-token dynamic quantization computes quantization parameters on-the-fly for each input token during inference. This approach incurs significantly higher computational overhead, as the quantization parameters must be recalculated for every input token, along with multiple additional memory traversals. Such requirements make per-token dynamic quantization unfriendly or impractical for edge devices and some AI accelerators, which struggle with fine-grained dynamic operations (Tan et al., 2024). This issue is especially severe in MLLMs, where the token count increases significantly with higher image resolution or more video frames. The Modality-Specific Static Quantization (MSQ) in MQuant is a novel per-modality quantization approach specifically designed to address the unique challenges of MLLMs quantization.

Furthermore, MSQ can be naturally applied to the unified modality-decoupled tokens generated by AIFS. By integrating MSQ and AIFS, our designs yields three key advantages: **(1) Computational Equivalence and Strong Compatibility:** The unified causal mask and token index introduced by AIFS preserves the inherent causal relationships among tokens, ensuring numerical equivalence during attention computations. Moreover, since AIFS requires only a one-time rearrangement of the input data (adjust causal mask and token index in offline), it does not alter the overall computation graph. This characteristic allows for seamless integration with other LLM inference acceleration methods, such as FlashAttention (Dao et al., 2022), ensuring both computational equivalence and strong compatibility. As shown in Table 2, MQuant achieves SOTA quantization performance across 5 mainstream MLLMs. **(2) Reduced Inference Latency:** MSQ not only addresses the substantial distributional differences between modalities but also mitigates the significant computational overhead and increased inference latency caused by the surge in token counts from higher image and video resolutions. As shown in Table 7, MSQ+AIFS significantly reduces latency from 2.057s to 1.1017s, closely matching the speed of the per-tensor static setting while maintaining near-lossless accuracy comparable to the original Float model. **(3) Enhanced Memory and Computational Efficiency:** By combining MSQ and AIFS, we convert mixed input tokens into unified, modality-decoupled tokens, eliminating the irregular memory operations (e.g., slice, concat, pad) introduced by directly applying MSQ. This transformation reduces memory consumption and improves efficiency of GEMM kernel, which would otherwise be compromised by the interleaved and non-fixed positions of visual and textual tokens. As shown in Table 11, MQuant can achieve up to 24.7% speedup and 152.9% memory savings.

A.11. Comparison of Different MLLMs: Input Pre-Process, LayerNorm Architecture in Vision Encoder, Model Parameters and Flops.

In this section, we compare the visual input pre-process methods, LayerNorm structures in MLLM vision encoder, model parameters, and Flops across five mainstream MLLMs: InternVL2-8B (Chen et al., 2024a), Qwen-VL-Chat-9.6B (Bai et al.,

Table 13: Comparison of TTFT sensitivity to image resolution, model Parameters and flops in mainstream MLLMs. † means the Flops values are measured with the number of visual tokens is 256.

MLLMs	TTFT’s sensitivity to input image resolution	LayerNorm	Params (B)		FLOPs (T)†	
			Visual	LLM	Visual	LLM
InternVL2-8B	TTFT increases with input image aspect ratio	Pre-LN	0.34	7.74	1.28	7.54
Qwen-VL-Chat-9.6B	Fixed input resolution (448×448)	Pre-LN	1.94	7.73	4.23	3.70
MiniCPM-V 2.6-8B	TTFT increases with input image aspect ratio	Pre-LN	0.49	7.61	4.16	3.64
Qwen2-VL-7B	TTFT increases quadratically with input image resolution	Pre-LN	0.68	7.61	1.31	3.61
GLM-4V-9B	Fixed input resolution (1120×1120)	Post-LN	4.51	8.78	12.10	4.70

2023b), MiniCPM-V 2.6-8B (Yao et al., 2024), Qwen2-VL-7B (Wang et al., 2024), and GLM-4V-9B (Hong et al., 2024). As shown in Table 13, this comparison highlights the architectural differences between these models, particularly the TTFT sensitivity to input image resolution, illustrating the unique challenges these variations present for quantization and efficient inference.

A.12. Quantization Granularity

Furthermore, as mentioned in SoomthQuant (Xiao et al., 2022), there are different different granularity levels. The **per-tensor static** quantization uses a single step size for the entire matrix. **Per-token dynamic** quantization employs different s for the activations associated with each token, being a common granularity for activations quantization of existing LLMs. For weights, per-channel quantization applies distinct s for each output channel of the weights, while group-wise quantization utilizes a coarse-grained s for different channel groups. Notably, group-wise quantization is a prevalent granularity for weight quantization in LLMs (Frantar et al., 2022; Yao et al., 2022). Please refer to appendix for more quantization basics.

A.13. LayerNorm, RMSNorm and Computational Invariance

We introduce LayerNorm, RMSNorm, the computational Invariance, and their usage in Transformers.

Layer Normalization (LayerNorm, LN) (Ba, 2016) is a technique to normalize the activations of intermediate layers of neural networks. Given a vector $\mathbf{x} \in \mathbb{R}^d$, LayerNorm normalizes it to obtain a zero-mean unit-variance vector,

$$\text{LayerNorm}(\mathbf{x}) = \frac{\mathbf{x} - \mu(\mathbf{x})\mathbf{1}}{\sqrt{\|\mathbf{x}\|_2^2/d - \mu^2(\mathbf{x}) + \epsilon}}, \text{ where } \mu(\mathbf{x}) = \frac{\mathbf{1}^T \mathbf{x}}{d}, \epsilon > 0. \quad (14)$$

LayerNorm recenters and rescales the activations and gradients in the forward and backward computations, which enables fast and robust training of neural networks.

Root Mean Square Normalization (RMSNorm) (Zhang et al., 2019) is another technique used for normalizing the activations. It is similar to LayerNorm in that it aims to accelerate and stabilize the training but uses a different normalization approach. Instead of normalizing the inputs based on their mean and variance, RMSNorm normalizes them based on their root mean square (RMS) value. It is defined in the following equation,

$$\text{RMSNorm}(\mathbf{x}) = \frac{\mathbf{x}}{\sqrt{\|\mathbf{x}\|_2^2/d + \epsilon}}, \text{ where } \epsilon > 0. \quad (15)$$

RMSNorm only rescales the input vector and the corresponding gradients, discarding the recentering process. As shown in their definitions, RMSNorm is computationally simpler and more efficient than LayerNorm. It is reported that replacing LayerNorm with RMSNorm can achieve comparable performance and save training and inference time by 7% – 64% (Zhang et al., 2019).

Given a zero-mean vector \mathbf{x} , these two kinds of normalization are equivalent. Formally, if $\mu(\mathbf{x}) = 0$, then $\text{LayerNorm}(\mathbf{x}) = \text{RMSNorm}(\mathbf{x})$. We may optionally introduce learnable parameters and apply an element-wise affine transformation on the output of LayerNorm and RMSNorm.

LayerNorm (LN) and RMSNorm Given the input concated token \mathbf{X} after embeddings with the shape $L \times D$, the \mathbf{X} is passed through a LayerNorm (Ba, 2016) operation, which subtracts the mean from each row of the matrix, divides the

row by its standard deviation, rescales (columnwise), and adds an offset. Follow (Ashkboos et al., 2024a), we write the LayerNorm block as

$$\text{LayerNorm}(\mathbf{X}) = \text{RMSNorm}(\mathbf{X}\mathbf{M})\text{diag}(\boldsymbol{\alpha})\sqrt{D} + \mathbf{1}_N\boldsymbol{\beta}^\top \quad (16)$$

where $\text{RMSNorm}(\mathbf{X})$ applies $\mathbf{x} \leftarrow \mathbf{x}/\|\mathbf{x}\|$ to each row of \mathbf{X} , and $\mathbf{X} = \text{concat}(\mathbf{E}_v, \mathbf{E}_t)$ is the concatenation between text tokens \mathbf{E}_t and the visual tokens \mathbf{E}_v . The vector parameter $\boldsymbol{\alpha}$ and offset (vector) parameter $\boldsymbol{\beta}$ are learned independently at each LayerNorm instance. The constant matrix $\mathbf{M} = \mathbf{I} - \frac{1}{D}\mathbf{1}\mathbf{1}^\top$ is a $D \times D$ matrix which subtracts the mean from each row of \mathbf{X} , called recentering operation. Formally, if $\mathbf{M} = \mathbf{I}$, the input \mathbf{X} has a zero-mean, the Eq 16 is equivalent to RMSNorm. Specifically, LayerNorm is widely employed in visual encoders E , whereas RMSNorm (Zhang et al., 2019) is commonly used in LLMs (Touvron et al., 2023a; Dubey et al., 2024) and has been shown to accelerate training and inference time with similar performance (Zhang et al., 2019).

Computational Invariance in RMSNorm. Based on the *computational invariance*, recent studies (Ashkboos et al., 2024a;b) have shown that orthogonal transformations can effectively smooth outliers and improve the quantize-ability of both weights and activations. In particular, for transformers, inserting linear layers with an orthogonal matrices \mathbf{Q} before and after the RMSNorm (Zhang et al., 2019) layer in a transformer, the network remains unchanged. In detail, given the input \mathbf{X} and orthogonal matrix \mathbf{Q} for RMSNorm layer, the *computational invariance* means: $\text{RMSNorm}(\mathbf{X}\mathbf{Q})\mathbf{Q}^\top = \text{RMSNorm}$. Here, $\mathbf{Q}^\top\mathbf{Q} = \mathbf{Q}\mathbf{Q}^\top = \mathbf{I}$ and a rotation matrix is an orthogonal matrix with $|\mathbf{Q}| = 1$. Note that multiplying a vector \mathbf{x} by \mathbf{Q} does not change the norm of the vector, since $\|\mathbf{Q}\mathbf{x}\| = \sqrt{\mathbf{x}^\top\mathbf{Q}^\top\mathbf{Q}\mathbf{x}} = \sqrt{\mathbf{x}^\top\mathbf{x}} = \|\mathbf{x}\|$.

A.14. LayerNorm to RMSNorm Transformation.

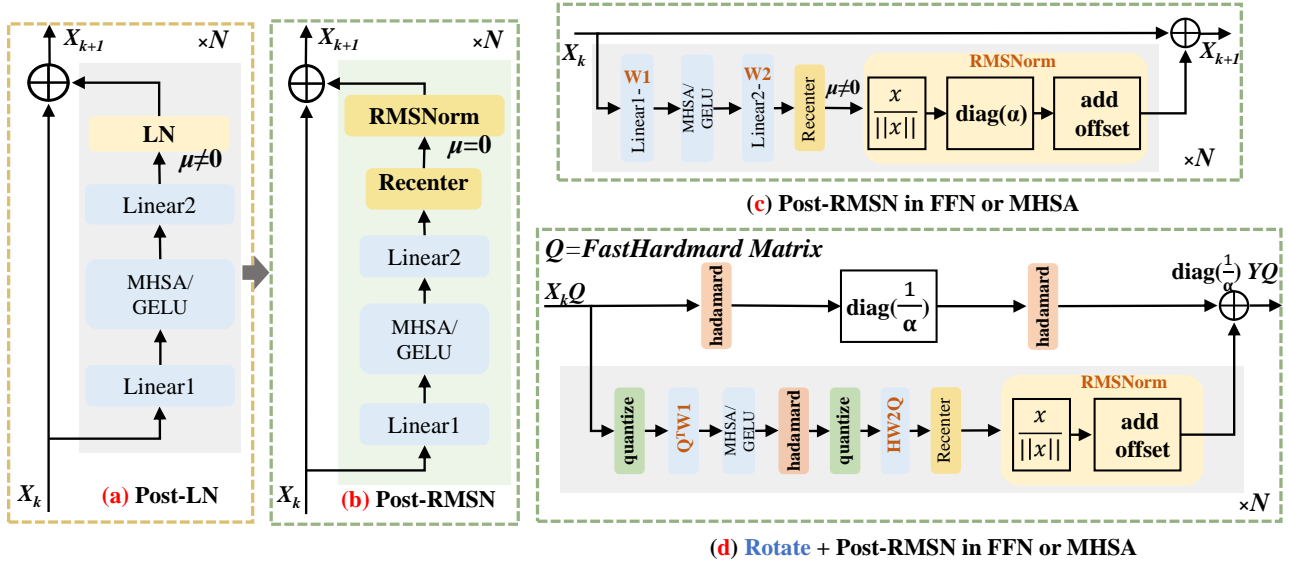


Figure 8: The proposed Post-LN + Rotate Scheme.

Post-LayerNorm to RMSNorm Transformation. As shown in Figure 8, we present the detailed Post-LN + Rotate design. Unlike the Pre-LN + Rotate in SliceGPT (Ashkboos et al., 2024a), our Post-LN + Rotate scheme extends the applicability for different MLLMs’ vision encoder.

Pre-LayerNorm to RMSNorm Transformation. Here, we propose unified LayerNorm-to-RMSNorm transformation, aiming to synthesize the transformer architecture of MLLMs’ vision encoders and LLMs, endowing them with rotation-friendly characteristics that facilitate the effective removal of outliers. We take Pre-LN transformer as an example to show that how transform Pre-LN into RMSNorm layer while guaranting arithmetic equivalence. As shown in Figure 9 (a), for the input \mathbf{X}_k of the k -th block, the main block in pre-LN transformer is $\mathbf{X}_{k+1} = \mathbf{X}_k + \ell_2(g(\ell_1(LN(\mathbf{X}_k))))$, where $k \in [1, N]$, and N is the block number. If g is an activation function, such as GELU, this block is a multi-layer perceptron (MLP) module. If g is a multi-head attention, then this block is the casual attention module (Vaswani et al., 2017). Due to the recentering operation, LN exhibits invariance to shifts, such that $LN(\mathbf{X}_k - a\mathbf{1}) = LN(\mathbf{X}_k), \forall a \in \mathbb{R}$.

Therefore, as shown in Figure 9 (b), we can replace LN as RMSNorm layer through two modifications: ❶ recenter the input \mathbf{X}_k to $\mathbf{X}_k - \mu(\mathbf{X}_k)\mathbf{1}$, ensuring that the input to norm layer maintain a zero mean. ❷ adjust the weights \mathbf{A}_2 and bias \mathbf{b}_2 of the the linear ℓ_2 to $\hat{\mathbf{A}}_2 = \mathbf{A}_2 - \frac{1}{D}\mathbf{1}\mathbf{1}^T\mathbf{A}_2, \hat{\mathbf{b}}_2 = \mathbf{b}_2 - \mu(\mathbf{b}_2)\mathbf{1}$. Consequently, the LN can be replaced with an RMSNorm layer with the same arithmetic functionality. The first operation is to recenter \mathbf{X}_k , while the second operation is to recenter the output of main branches. Notably, since $\mathbf{X}_{k+1} = \mathbf{X}_k + \ell_2(g(\ell_1(LN(\mathbf{X}_k))))$, after applying ❶ and ❷, the input and the output of main branch are re-centered with zero-mean, while the input of residual branches also maintain a zero mean. Therefore, the output after current blocks, \mathbf{X}_{k+1} (which serves as the input for next block), still maintain zero-mean. A detailed proof is provided in the Appendix. Ultimately, we establish the equivalence of Pre-LN and Pre-RMSNorm Transformers. Now that every LayerNorm in the transformer has been converted to RMSNorm in MLLMs, we can use any orthogonal matrices \mathbf{Q} to the model. Therefore, the visual encoder and LLMs are in a rotation-friendly RMSNorm-only transformer architecture.

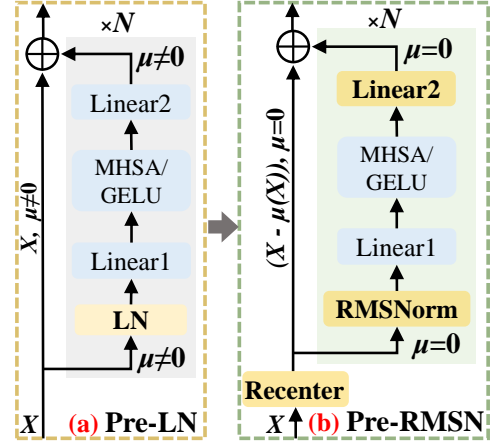


Figure 9: The illustration of transformation from Pre-LN to RMSNorm.